Electrochemical Investigation of Crinum Asiaticum-Like BaO-CeO_2 nanostructure for High-Performance Asymmetric Supercapacitors

Rushikesh G. Bobade [a], Bidhan Pandit [b], Akhil P. Khedulkar [c], Vijay S. Raykar [d], Pradip B. Sarawade [e], Shoyebmohamad F. Shaikh [f], Chun Huang [b,g,h], Revanappa C. Ambare [a, *]

[a] *Department of Physics, KMC, College, Khopoli-410203, Raigad (Affiliated to University of Mumbai), Maharashtra, India.*

[b] *Department of Materials, Imperial College London, London SW7 2AZ, United Kingdom.*

[c] *Department of Electrophysics, National Yang Ming Chiao Tung University, 1001 University Road, Hsinchu 300093, Taiwan.*

[d] *Department of Physics, G.M. Vedak College of Science Tala Raigad 402111, (Affiliated to University of Mumbai), Maharashtra, India.*

[e] Physics, Advanced Materials & Energy Research (AMER) Laboratory, Mumbai University, Mumbai 400098, M.S., India

[f] *Department of Chemistry, College of Science, King Saud University, P.O. Box 2455, Riyadh 11451, Saudi Arabia.*

[g] *The Faraday Institution, Quad one, Becquerel Ave, Harwell Campus, Didcot, OX11 0RA, United Kingdom.*

[h] *Research Complex at Harwell, Rutherford Appleton Laboratory, Didcot, OX11 0FA, United Kingdom.*

[*]**Corresponding author:**

Dr. R.C. Ambare,

E-mail address: revanambare@gmail.com

Abstract

In this study, barium oxide-cerium oxide ($BaO\text{-}CeO_2$) thin films with a Crinum asiaticum flower-like morphology were fabricated using the sequential ionic layer adsorption and reaction (SILAR) technique. X-ray diffraction (XRD) analysis confirmed their polycrystalline structure, while structural, elemental, and compositional studies validated their suitability as electrode materials for supercapacitors. The $BaO\text{-}CeO_2$ thin films exhibited excellent electrochemical stability and high performance, achieving a specific capacitance (SC) of 880 F/g in a 1 M potassium hydroxide (1M KOH) electrolyte, with 97 % capacitance retention after 6,500 cycles. When assembled into an asymmetric solid-state supercapacitor device (ASSD), the electrodes delivered an energy density of 17.8 Wh/kg and a power density of 6.9 kW/kg, maintaining 98 % capacitance over 5,500 cycles. The ASSD successfully powered a green light-emitting diode, demonstrating its economic feasibility and practical potential for cost-effective energy storage applications.

Keywords: $BaO\text{-}CeO_2$, Electrode, Morphology, SILAR, Supercapacitor, Thin film.

1. Introduction

In recent decades, supercapacitors have emerged as promising electronic devices for energy storage applications, yet they encounter various challenges due to their compact form, enhanced electrical conductivity, rapid charge-discharge cycles, and prolonged stability characteristics, bridging the gap between capacitors and batteries [1–4]. Today, a range of binary metal oxide thin-film electrodes are employed in energy storage solutions due to their exceptional features, such as higher energy as well power densities, compact configurations, as well robust cycling durability. In this study, barium oxide-cerium oxide (BaO-CeO_2) composite thin films are selected for supercapacitor applications, as they offer superior electrochemical performance compared to individual metal oxides [5–8].

The Barium oxide (BaO) is a highly effective electrical conductor, a critical attribute for electrode materials used in supercapacitors [9,10]. Enhanced conductivity within the electrode material supports efficient charge transfer, facilitating rapid charge and discharge cycles a key requirement for supercapacitors, which depend on fast energy storage and release. BaO also demonstrates remarkable chemical resilience, even in challenging operating environments. It resists corrosion and can operate across a broad pH spectrum, maintaining durability through extensive cycling, which is vital for the long-term reliability of supercapacitors [11–13].

The Cerium oxide (CeO_2) nanoparticles, synthesized with a high specific surface area, are similarly advantageous [14,15]. In supercapacitor applications, this expanded surface area increases the electrode-electrolyte interface, enabling a higher frequency of electrochemical reactions [16,17]. The larger surface area contributes to elevated capacitance, thereby enhancing the energy storage capacity. CeO_2 nanoparticles also exhibit strong electrochemical stability, allowing them to withstand prolonged cycling by resisting reactions with the electrolyte and maintaining their structural integrity through multiple charge-discharge cycles [18–20]. With

cerium being relatively abundant, CeO_2 nanomaterials are cost-effective to synthesize, supporting their potential for scalable supercapacitor production and commercial feasibility [21–24].

The BaO-CeO_2 nanocomposites integrate the advantageous characteristics of both BaO and CeO_2, such as the high electrical conductivity from BaO and the excellent redox activity of CeO_2 [25,26]. This combination produces a synergistic effect that enhances electrochemical performance, including increased capacitance and energy density compared to single-component electrodes. BaO-CeO_2 mixed-phase nanocomposites demonstrate superior chemical and electrochemical stability relative to individual BaO or CeO_2 electrodes, an essential feature for sustaining performance over prolonged cycling and numerous charge-discharge cycles [27–29].

The interaction of BaO and CeO_2 in these nanocomposites improves charge transport properties by creating a conductive network through CeO_2, which facilitates electron mobility within the composite, while BaO enhances ion transport pathways [30,31]. This combined effect supports faster charge and discharge rates. The BaO-CeO_2 nanocomposites exhibit pseudocapacitive behavior due to the redox capabilities of CeO_2, which contributes to a greater energy storage capacity beyond that of purely electric double-layer capacitance [32–34]. The synthesis of BaO-CeO_2 mixed-phase nanocomposites is typically scalable and cost-efficient, which is beneficial for large-scale production and potential commercial applications. By combining the strengths of BaO and CeO_2, these composites overcome individual material limitations, resulting in improved electrochemical performance, enhanced stability, and versatility [35–37]. Such advantages position BaO-CeO_2 nanocomposites as promising candidates for supercapacitor electrode materials. Recently, Sadeghinia *et al.* [11] got PANI/PBF-NPs electrodes by a hydrothermal technique that obtained 310 F/g SC at 5 mV/s. Padmadevi *et al.* [12] produced MnO_2-CuO-BaO, by a hydrothermal technique, with a maximum SC of 198 F/g in 1M KOH.

Shanmugavadivel *et al.*[13] manufactured $BaMnO_3$ hydrothermally this offered cycling durability of 93.9% capacitance holding afterward 500 redox cycles, as well SC of 73.1 F/g. Prasannaa *et al.*[16] synthesied a CeO_2 electrode that established a 134.6 F/g SC with good capacitance holding of 92.5% capacitance after 1000 cycles. Ojha *et al.* [17] obtained CeO_2-MnO_2/RGO nanorod-like morphology that showed 315.13 F/g SC at a sweep rate of 5 mV/s in 1M KOH. Vanitha *et al.* [21] produced MgO: V electrode by a simple cost-effective hydrothermal technique SEM image shows rippled silk veil waves-like morphology with 710.42 F/g. Jeyaranjan *et al.* [22] Synthesis of nano-spears like PANI/rGO/CeO_2 by hydrothermal method shows 92% capacitance retention after 6000 cycles.

Among chemical methods, the Successive Ionic Layer Adsorption and Reaction (SILAR) technique is recognized as an eco-friendly approach for synthesizing thin-film electrodes layer-by-layer. It enables the formation of uniform films at room temperature, and in the current study, it has been employed to synthesize BaO-CeO_2 films with a Crinum asiaticum-inspired flower-like morphology [38–40].

2. Experimental

2.1 Materials

Cerium (III) nitrate (Ce $(NO_3)_3.6H_2O$) (99% extra pure), barium nitrate (Ba $(NO_3)_2$) (99% extra pure), Sodium hydroxide pallets (NaOH) (98% extra pure), potassium hydroxide [KOH], sulphuric acid (H_2SO_4), acetone, and polyvinyl alcohol (PVA). All chemicals have acquired from Merck Private Ltd as well used without using additional purification. Stanless still (SS) has used as a conducting substrate.

2.2 Synthesis of BaO

The synthesis of the BaO was carried out using a 0.05 M solution of $Ba(NO_3)_2$ as a cationic

solution as well a 1 M NaOH solution as an anionic solution. A preparation process involved four main steps: (a) immersing the stainless steel (SS) substrate in the $Ba(NO_3)_2$ solution for 60 seconds to enable Ba^{2+} ions to adhere to the conductive surface, (b) rinsing the substrate in deionized water (DW) for 20 seconds to wash away loosely bound barium ions, (c) immersing the substrate in the NaOH solution for 60 seconds to form a layer of barium hydroxide, and (d) repeating the rinsing step to remove any weakly attached ions or molecules. This sequence constitutes 1 SILAR cycle, and a consistent barium hydroxide layer has achieved after approximately 90 cycles. The resulting film was air-dried at 30°C and subsequently annealed in the muffle furnace at 573 K for 1 hour to obtain the BaO thin film, designated as a Ba_{300} electrode sample [41–43].

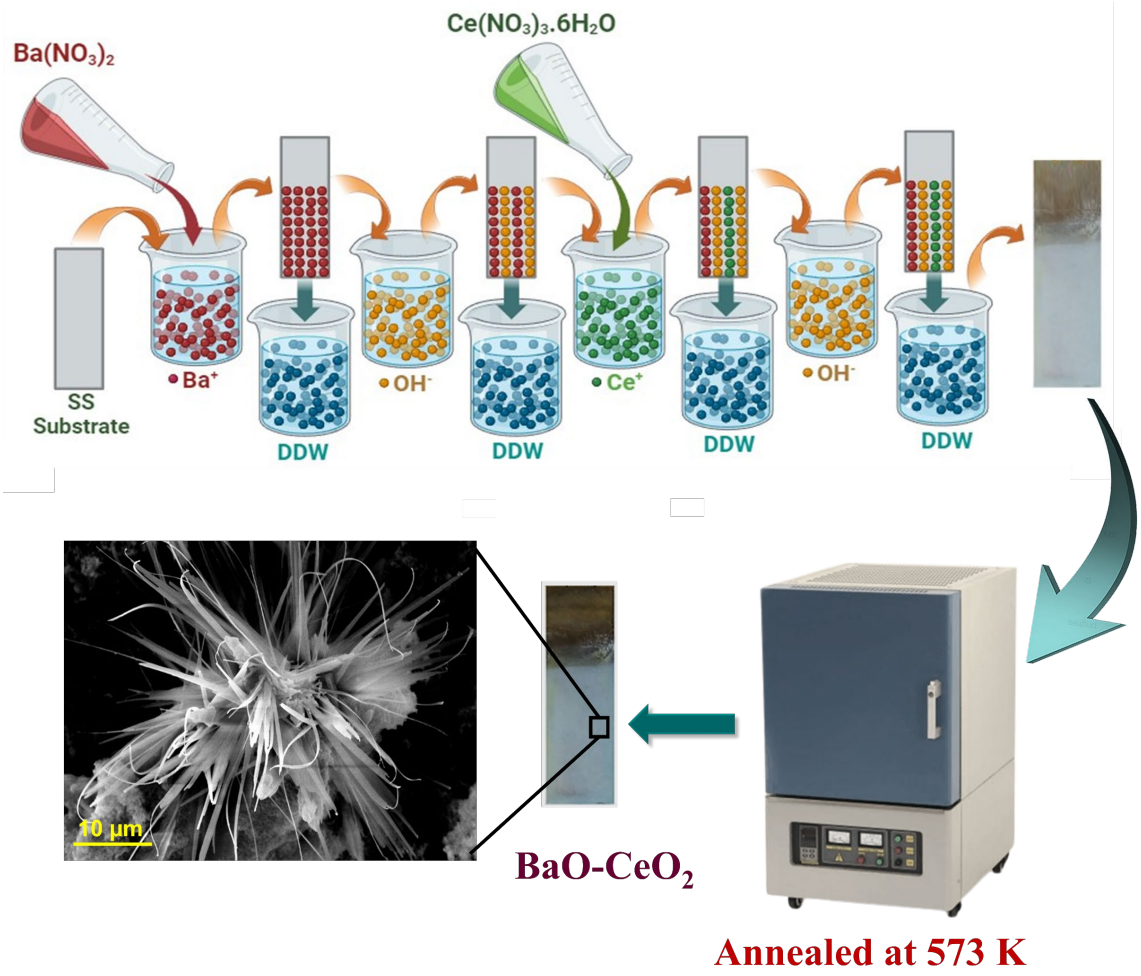
2.3 Synthesis of CeO_2

To fabricate the CeO_2 thin films, a SS conductive substrate was alternately immersed in 0.05 M $Ce(NO_3)_3$ and 1 M NaOH solutions, followed by rinsing after each immersion. The process consisted of four primary steps: (a) a SS substrate has submerged for 60 seconds in 10 ml of deionized water (DW) containing 0.05 M $Ce(NO_3)_3$ solution, allowing Ce^{3+} ions to adhere to a surface, (b) a substrate has then rinsed in DW for 20 seconds to remove any weakly attached cerium ions, (c) it was subsequently immersed in 10 ml DW containing 1 M NaOH solution for 60 seconds to allow a Ce^{3+} ions to react with OH^- ions, forming a cerium hydroxide layer, and (d) rinsing was repeated to eliminate loosely bound OH^- ions, completing 1 SILAR cycle. To accomplish a uniform layer, nearly 90 cycles were conducted, resulting in a consistent cerium hydroxide film on a SS substrate. This film was then annealed in the muffle furnace at 573 K for about one hour, yielding the CeO_2 thin film, designated as the Ce300 electrode sample [41–43].

2.4 Synthesis and reaction kinetics of BaO-CeO_2 thin film formation

The composite BaO/CeO_2 thin film has deposited on a SS substrate by the SILAR method.

For an anionic source, a 1 M NaOH solution was used to supply OH^- ions, while 0.05 M solutions of barium nitrate as well cerium nitrate acted as cationic sources for Ba^{2+} and Ce^{3+} ions, respectively. A deposition process involved multiple steps: (a) immersing the SS substrate for 60 seconds in 10 ml of deionized water (DW) containing 0.05 M $Ba(NO_3)_2$ to allow Ba^{2+} ions to adhere, (b) rinsing the substrate in DW for 10 seconds to wash away loosely attached Ba^{2+} ions, (c) submerging it in 10 ml of DW with 1 M NaOH for 60 seconds to facilitate OH^- ions bonding with Ba^{2+} ions and forming a barium hydroxide layer, (d) repeating the rinse to remove unattached OH^- ions, (e) immersing the substrate in a 0.05 M $Ce(NO_3)_3.6H_2O$ solution for 60 seconds to add cerium ions, creating a barium-cerium layer, (f) rinsing to dislodge any loosely bound barium-cerium ions, (g) placing the substrate in 10 ml of 1 M NaOH solution for 60 seconds, allowing OH^- ions to react with a deposited ions to form a barium-cerium hydroxide layer, and (h) a final rinse to remove any weakly attached ions, completing one SILAR cycle. Repeating this SILAR cycle 90 times produced a uniform barium-cerium hydroxide layer on the SS substrate, which was then annealed in a muffle furnace at 573 K for one hour, yielding a composite barium oxide-cerium oxide ($BaO\text{-}CeO_2$) thin film, designated as the $Ba\text{-}Ce_{300}$ electrode sample [44–47].



Schematic 1: Schematic shows the formed BaO-CeO_2 nanocomposites electrode.

The schematic representaion of a SILAR technique used to synthesis of BaO-CeO_2 electrode is revealed in **Schematic 1**. The possible chemical reaction given as following:

$$Ba(NO_3)_2 + Ce(NO_3)_3.6H_2O + H_2O \longrightarrow Ba^{2+} + Ce^{3+} + 5NO_3^- + 7H^+ + 7OH^- \quad (1)$$

$$NaOH + H_2O \longrightarrow Na^+ + 2OH^- + H^+ \quad (2)$$

$$Ba^{2+} + 2OH^- \longrightarrow Ba(OH)_2 \quad (3)$$

$$Ce^{3+} + 3OH^- \longrightarrow Ce(OH)_3 \quad (4)$$

$$2Ba(OH)_2 + 2Ce(OH)_3 + O_2 \xrightarrow{(573\ K)} 2(BaO - CeO_2) + 5H_2O \uparrow + \frac{1}{2}O_2 \quad (5)$$

2.5 Electrochemical measurements

The electrochemical characteristics of BaO-CeO_2 composite thin films were investigated by CV, CP, and EIS. The three electrode system was employed to assess the electrochemical performance in a 1 M KOH solution, with the BaO-CeO_2 composite films serving as a working electrode, platinum as a counter electrode, and Ag/AgCl as the reference electrode [48,49]. Charging-discharging behaviors were examined at dissimilar current densities within a same potential range, and CV measurements were carried out at varying sweep rates within a potential range of -1.3 to 0.4 V, with an alternating current amplitude of 10 mV and a bias voltage of 0.4 V. EIS has performed over a frequency ranging of 1 Hz to 100 kHz to evaluate the impedance characteristics of the electrode.

$$SC = \frac{1}{mv\,(v_f - v_i)} \int_{v_i}^{v_f} I\,(V)\,dv \tag{6}$$

$$SE = \frac{V \times I_d \times t_d}{m} \tag{7}$$

$$SP = \frac{V \times I_d}{m} \tag{8}$$

Where, "SC" specific capacitance in F/g, "(V_f - V_i)" potential window, 'm' active mass on electrode, 'v' sweep rate in mV/s, "$\int_{v_i}^{v_f}$ " integral area under of CV curve, "SE" energy density in Wh/kg, "SP" power density in kW/kg, "V" applied potential in volt, 'I (V)' current in mA, 'I_d' discharg current, and 't_d' discharging time in second.

2.6 Fabrication of BaO-CeO_2//Activated Carbon asymmetric devices

Activated carbon (AC) and BaO-CeO_2 nanocomposite electrodes have employed as a positive as well negative electrodes, correspondingly. A Filter paper was used to separate the two electrodes, while a PVA-KOH gel acted as the electrolyte. In our recent studies [50,51], we discussed the fabrication of devices, the preparation of activated carbon electrodes, and the

synthesis of PVA-KOH gel. After immersion in the gel electrolyte for 10 seconds, the electrodes and separator paper were air-dried at 30°C for 1 hour. Before assembling the device, the thin film electrode was coated with PVA-KOH gel and dried for 6 to 8 hours at 30° to 35°C in an electric oven to eliminate any absorbed water from the surface. To improve an interaction among a electrolyte as well the electrode surface, the asymmetric device was fabricated by applying pressure to the coated region of the electrodes for 1 hour [52].

2.7 Computational details

A density functional theory-based first-principal calculation was performed to calculate the electronic properties of BaO and CeO_2 using Quantum Espresso [53]. The Generalized Gradient Approximation (GGA) has used to deal with exchange and correlation energy. A plain wave basis set of cutoff energy 816 eV was used. The k-points mesh of 10×10×10 with Monkhorst-Pack sampling was used for structural optimization and Self-consistent field (SCF) calculation. The fully optimized structures with forces less than 0.0026 eV/Å were used to calculate the structural and electronic properties.

3. Results and Discussions

3.1 X-ray diffraction analysis

A formation of BaO, CeO_2, as well BaO-CeO_2 composite nanomaterials was analyzed using XRD patterns. A XRD of BaO, CeO_2, and a BaO-CeO_2 composite films, fabricated on the SS substrate by a SILAR technique, are presented in Fig. 1. In **Fig. 1 (a)**, the XRD pattern of the Ba_{300} sample displayed peaks at 19.7°, 24.1°, 34.7°, 39.6°, 42.1°, 44.9°, 46.9°, and 64.5°, which were assigned to the (200), (201), (212), (111), (200), (002), (103), and (202) planes (JCPDS No. 26-0178) of tetragonal BaO. These peak positions were consistent with previous findings described by Ansari *et al.* [54]. The **Fig. 1 (b)** shows a XRD pattern for a Ce_{300} sample (JCPDS No. 34-

0394), which exhibited distinct sharp peaks at 28.5°, 43.5°, 75.1°, and 90.8°, consistent to a (111), (220), (331), and (422) planes, indicating the presence of CeO2 with a cubic crystal structure, like to the observations by Lee *et al* [16]. No secondary phases were observed in either XRD plot. In **Fig. 1 (c)**, the XRD pattern of the Ba-Ce_{300} composite displayed well-defined peaks at 19.5°, 24.1°, 28.7°, 34.7°, 39.6°, 42.1°, 44.7°, 46.9°, 64.9°, 75.1°, and 90.8°, which matched the (200), (201), (111), (212), (111), (200), (002), (103), (202), (331), and (422) planes, confirming the successful formation of the BaO-CeO_2 composite. A crystallite size "D" has calculated using Scherrer's equation [55,56].

A crystalline size "D" has determined by Scherrer's formula.

$$D = \frac{K\lambda}{\beta \cos\theta} \tag{9}$$

Where, 'K' constant (0.9), 'λ' wavelength of X-ray, 'β' full-width half maximum (FWHM), and 'θ' Bragg's angle.

A crystallite sizes of the Ba_{300}, Ce_{300}, and Ba-Ce_{300} electrode composites have approximately ≈31 nm, ≈27 nm, and ≈14 nm, correspondingly. As shown in **Fig. 1 (d & e)**, the crystal structures of BaO and CeO_2 exhibited layered arrangements, which provided efficient pathways for electrolyte ions to undergo intercalation and extraction processes, significantly enhancing electrochemical performance. The formation of the BaO-CeO_2 composite thin films, including nucleation and stabilization effects at the nanoscale, led to reduced crystallite sizes compared to the individual BaO and CeO_2 materials, as seen in the XRD data. This reduction in crystalline size contributed to improved electrochemical properties. The micro-strain was determined by a following formula [57,58].

$$\varepsilon = \frac{\beta}{4\tan\theta} \tag{10}$$

A calculated microstrain values for the Ba_{300}, Ce_{300}, and Ba-Ce_{300} composite films were

approximately 0.0269, 0.0274, and 0.0348, respectively. The BaO coating in the Ba_{300} sample exhibited a relatively well-ordered structure with minimal lattice distortions, as indicated by its low microstrain value. In contrast, the Ce_{300} sample showed some variations in lattice structure compared to BaO, which likely contributed to lattice strain as well distortions, resulting in slightly higher microstrain. The Ba-Ce_{300} composite electrode demonstrated that an incorporation of CeO_2 into a BaO lattice led to more significant lattice distortions, yielding a higher microstrain value compared to the individual BaO as well CeO_2 thin films.

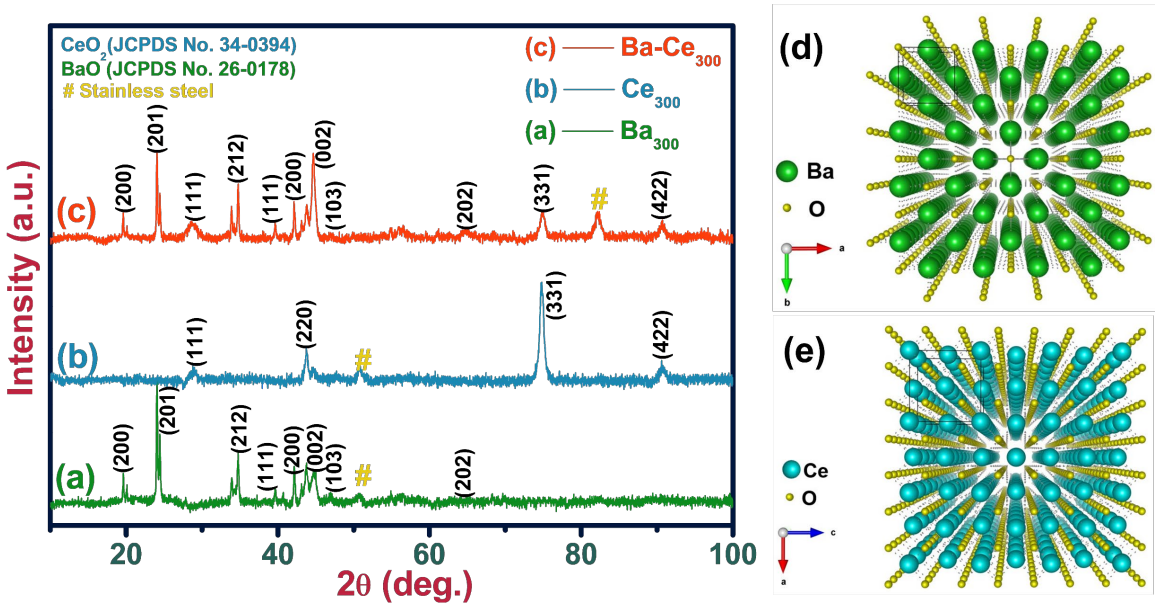


Fig. 1: X-ray diffraction patterns of sample electrode (a) Ba_{300}, (b) Ce_{300}, (c) Ba-Ce_{300}, the corresponding crystal structure of (d) BaO, and (e) CeO_2.

3.2 XPS analysis

X-ray photoelectron spectroscopy (XPS) is employed to determine an elemental composition as well oxidation states of Ce, Ba, O, and C in an active materials. The survey spectrum for the Ba-Ce_{300} composite is displayed in **Fig. 2(a)**, where a binding energies of Ce 3d, Ba 3d, O 1s, and C 1s were found to be 902.8, 785.1, 534.6, and 286.8 eV, respectively. The Ce

3d XPS spectrum, as shown in **Fig. 2(b)**, revealed three distinct peaks, which is characteristic of Ce, making its analysis more complex [59–61]. While the expected Ce^{5+} (3d-l) ionized state could have been observed, the Ce^{4+} (3d-l4f1) state was found to be more stable. This was due to electron transfer from a valence O 2p orbitals to a Ce 4f orbitals, indicating that the valence state of Ce in the composite was a two-electron transition, corresponding to Ce^{4+} (3d-l4f1). This was further confirmed by the triplet of $3d_{3/2}$ and $3d_{5/2}$ peaks in the Ce 3d spectrum, which were fitted using CASA-XPS software, yielding results consistent with previous studies [62,63].

The Ba 3d spectra revealed in **Fig. 2(c)** revealed 2 distinct peaks corresponding to the Ba $3d_{5/2}$ as well Ba $3d_{3/2}$ lines at binding energies of 783.1 eV as well 798.4 eV, correspondingly. An energy separation of 15.4 eV between these two peaks suggests that Ba is in the 2+ oxidation state, as observed for BaO, which is consistent with literature findings [64]. The O 1s spectrum in **Fig. 2(d)** exhibited a broad feature, indicating a presence of lattice oxygen species in the Ba-Ce_{300} composite, through the full width at half maximum (FWHM) of 2.2 eV. This broadening can be attributed to the contribution from CeO_2, which has been reported to exhibit a shift in an O 1s binding energy from 531.7 eV to 533.9 eV upon modification of CeO_2 [65]. The shift and increased FWHM further support the presence of oxygen vacancies within the CeO_2 lattice.

The C 1s spectrum, showed in **Fig. 2(e)**, showed a peak at 286.8 eV, which corresponds to the carbon species in the sample. The binding energy values were influenced by the electronegativity of the surrounding atoms, with C-O species (hydroxyl, epoxide) showing higher binding energies than singly bound oxygen species. The peaks at 288.6 eV and 293.1 eV correspond to contributions from C-O and C=O groups, respectively, such as those found in ketones, aldehydes, and carboxylic acids [66]. The XPS valence band (VB) spectrum in **Fig. 2(f)** revealed the valence band edge of the Ba-Ce_{300} electrode at 2.28 eV, providing insights into the

electronic structure and charge transfer characteristics of the material.

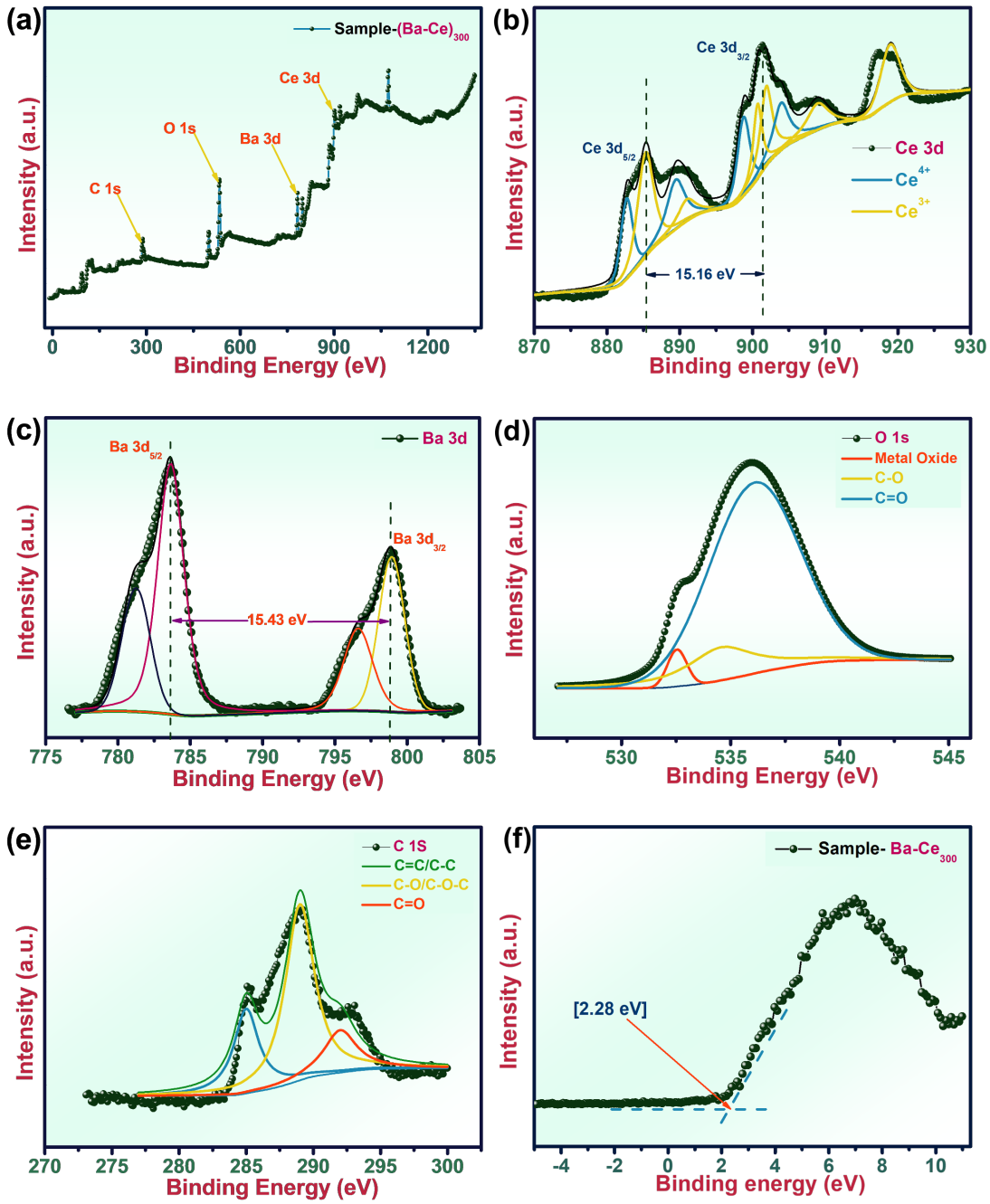


Fig. 2: (a) Survey spectra of sample Ba-Ce_{300}, deconvoluted XPS of (b) Ce 3d, (c) Ba 3d, (d) O 1s, (e) C 1s, (f) XPS valance band spectra of sample Ba-Ce_{300}.

3.3 FE-SEM and TEM analysis

The **Fig. 3(a & b)** present a FE-SEM images of a Ba_{300} sample at varying magnifications. At a lower magnification (10 μm), interconnected nanorods are clearly visible, while at higher magnification (1 μm), the particles are consistently distributed over a surface of a SS substrate, as observed by Suresh *et al.* [67]. The surface morphology of a Ce_{300} sample, revealed in **Fig. 3(c & d)** at 10 μm and 1 μm, revealed a consistent arrangement of closely packed nanospheres, similar to the observations made by Jayakumar *et al.* [68]. The Ba-Ce_{300} composite, as illustrated in **Fig. 3(e)**, exhibited a crinum asiaticum flower-like morphology, while in **Fig. 3(f)**, the BaO-CeO_2 mixed-phase nanoparticles presented an island-like configuration. These nanoparticles also demonstrated a uniform distribution in both size and shape, consistent with the findings of Zhang *et al.* [69]. The contact angle measurements shown in the insets of **Fig. 3(b), 3(d),** and **3(f)** revealed that the Ba_{300}, Ce_{300}, and Ba-Ce_{300} electrodes had contact angles of 65°, 60°, and 28°, respectively, confirming their hydrophilic nature. This suggests that the hydrophilic surfaces promote efficient ionic transport, which likely reduces a charge transfer resistance at an electrolyte-electrode boundary.

A **Fig. 4(a)** displays the elemental mapping images for O, Ba, and Ce. The elemental mapping of the Ba-Ce_{300} sample, shown in **Fig. 4(b & d),** confirms that all 3 elements, Ce, Ba, and O, are extant as well uniformly distributed across the Ba-Ce_{300} electrode. An Energy Dispersive X-ray (EDX) spectrum of a Ba-Ce_{300} sample is provided in **Fig. (S1)**, and the corresponding weight and atomic percentages for Ce, Ba, and O are listed in **Table (S1)**, showing values of 27.97%, 22.56%, and 49.47% by weight, and 5.78%, 4.76%, and 89.47% by atomic percentage, respectively. To gain further insights, Transmission Electron Microscopy (TEM) images of a Ba-Ce_{300} have exposed in **Fig. 4(e & f)**. At a inferior magnification (200 nm), **Fig. 4(e)** reveals the presence of black nanospheres, indicating that these nanoparticles have formed a

densely packed structure. At the higher magnification (100 nm), **Fig. 4(f)** shows that the nanoparticles have aggregated across a SS substrate, further confirming their compact nature.

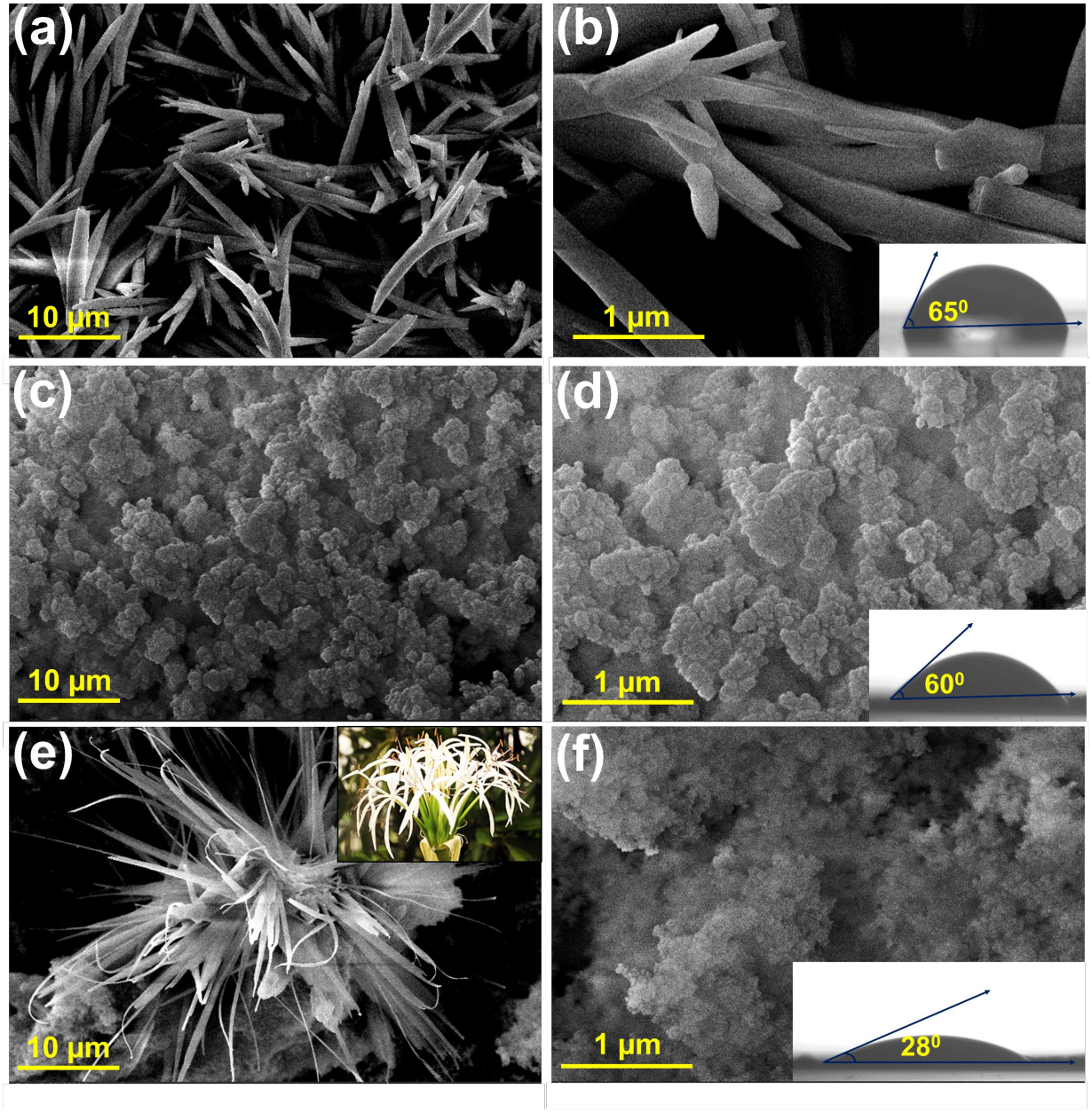


Fig. 3: FE-SEM images of a samples (a, b) Ba_{300}, (c, d) Ce_{300}, and (e, f) Ba-Ce_{300} at dissimilar magnifications, instead of (e) image of crinum asiaticum flower, wettability image inset of a sample (b) Ba_{300}, (d) Ce_{300}, (f) Ba-Ce_{300}.

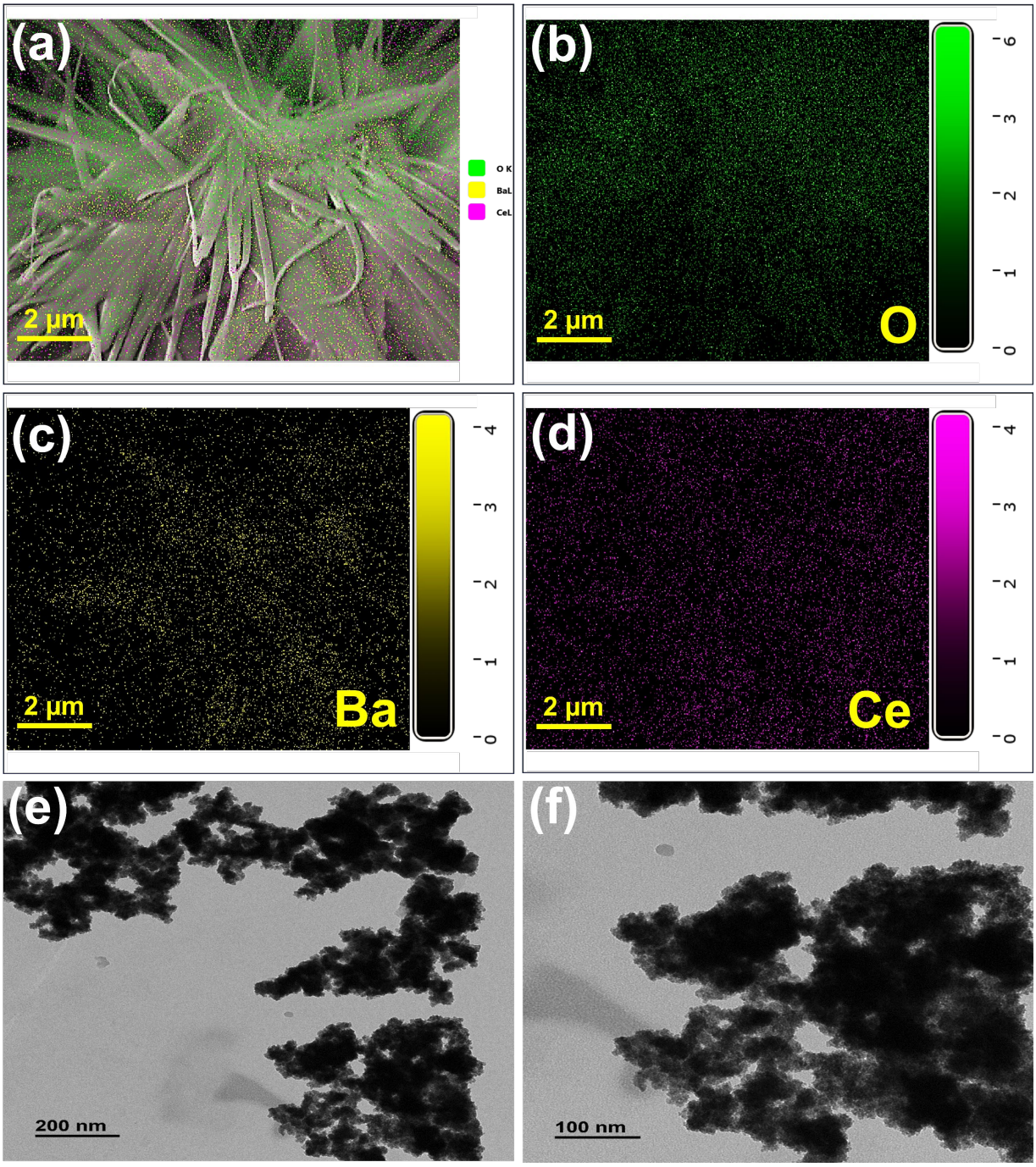


Fig 4: The EDAX images of (a) Sample Ba-Ce_{300}, (b) O, (c) Ba, (d) Ce, TEM images of scratch BaO-CeO_2 composite nanomaterial of sample Ba-Ce_{300} at (e) 200 nm, and (f) 100 nm.

3.4 Theoretical insights

Before investigating electronic property, the structure of BaO and CeO_2 are fully

optimized. The lattice constants of optimized BaO with space group P4/nm and CeO_2 with space group $Fm\bar{3}m$ are $a = b = 4.729$ Å, $c = 3.943$ Å and $a = b = c = 5.468$ Å. The band diagram of BaO is shown in **Fig. 5 (b)**, the valance band maxima is lies between Γ and M points and the conduction band minima is at Γ point, which makes BaO an indirect band gap semiconductor by band gap 2.84 eV. While in case of CeO_2, the valance band maxima are found at X point as well conduction band minima is at L-point, and a band gap is 1.85 eV, indicating CeO_2 is also an indirect band gap semiconductor as displayed in **Fig. 5 (d)**. To further check the atomic contribution in valance and conduction band, PDOS is calculated. It is clearly visible in **Fig. 5 (a)** and **Fig. 5 (c)** that the Density of States (DOS) of O atom in BaO and CeO_2 majorly contribute to total density of states for valance band. While in conduction band major contribution is due to the Ba and Ce atom.

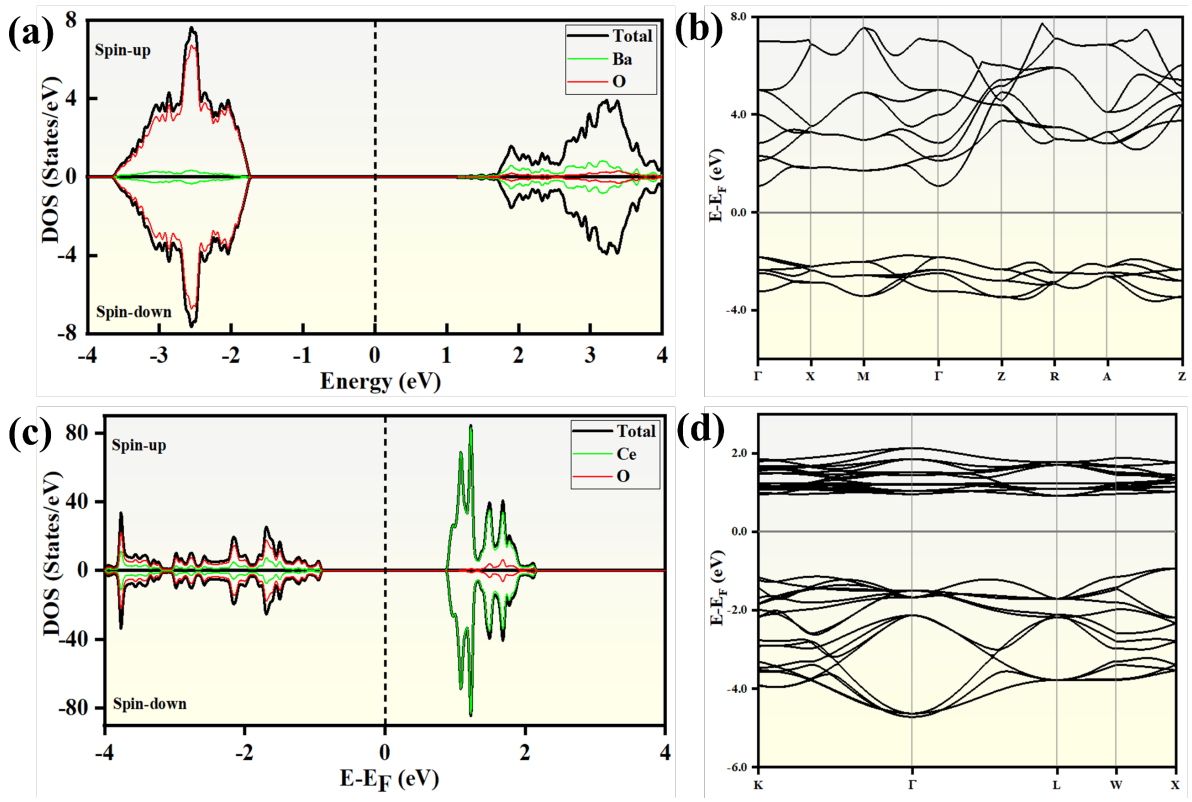


Fig 5: (a) Density of states of BaO, (b) Band diagram of BaO, (c) Density of states of CeO_2, (d)

Band diagram of CeO_2.

3.5 Supercapacitive analysis

3.5.1 Cyclic voltammetry (CV) study

After confirming a structural, morphological, as well compositional characteristics of a BaO-CeO_2 films, electrochemical measurements were performed to assess their supercapacitive behavior. The CV, CP, and EIS have utilized to evaluate an electrochemical performance of a Ba_{300}, Ce_{300}, and Ba-Ce_{300} electrodes using a three-electrode setup. The CV curves, obtained from -1.3 to 0.4 V potential at a sweep rate of 5 mV/s in 1M KOH, displayed distinct peaks, which emphasize the importance of composite electrodes for supercapacitor applications. These peaks, corresponding to anodic and cathodic sweeps, indicate an involvement of faradaic redox processes at an electrode-electrolyte interface, demonstrating the pseudocapacitive behavior of an electrodes shown in **Fig. 6 (a)**. The Ba-Ce_{300} electrode exhibited a significantly larger internal surface area compared to Ba_{300} and Ce_{300} electrodes, resulting in higher specific capacitance at 5 mV/s, suggesting its superior performance for energy storage applications.

The CV curves for Ba-Ce_{300} were also analyzed at various sweep rates ranging from 2-100 mV/s within the -1.3 to 0.4 V potential window in 1M KOH electrolyte shown in **Fig. 6 (b)**. At scan rates of 2-100 mV/s, the specific capacitance values were recorded as 880, 751, 655, 851, 512, and 473 F/g, respectively, with a clear reduction in capacitance as the scan rate increased shown in **Fig. 6 (c)**. This change was accompanied by a shift in a anodic as well cathodic peaks, highlighting the pseudocapacitive performance of a Ba-Ce_{300} electrodes. The interconnected island-like structure with a homogeneous distribution of nanostructures provided a larger active surface area, improving ion exchange and overall electrochemical performance [70,71]. As the sweep rate increased, the contribution of the diffusion process decreased, with the capacitance-

controlled contribution being highest at lower scan rates, as shown by the increasing capacitive contribution from 25.2 % at 2 mV/s to 84.1 % at 100 mV/s. These results underscore a impact of scan rate on the performance of composite electrodes, demonstrating their potential for higher performance supercapacitors shown in **Fig. 6 (d-f)** [72].

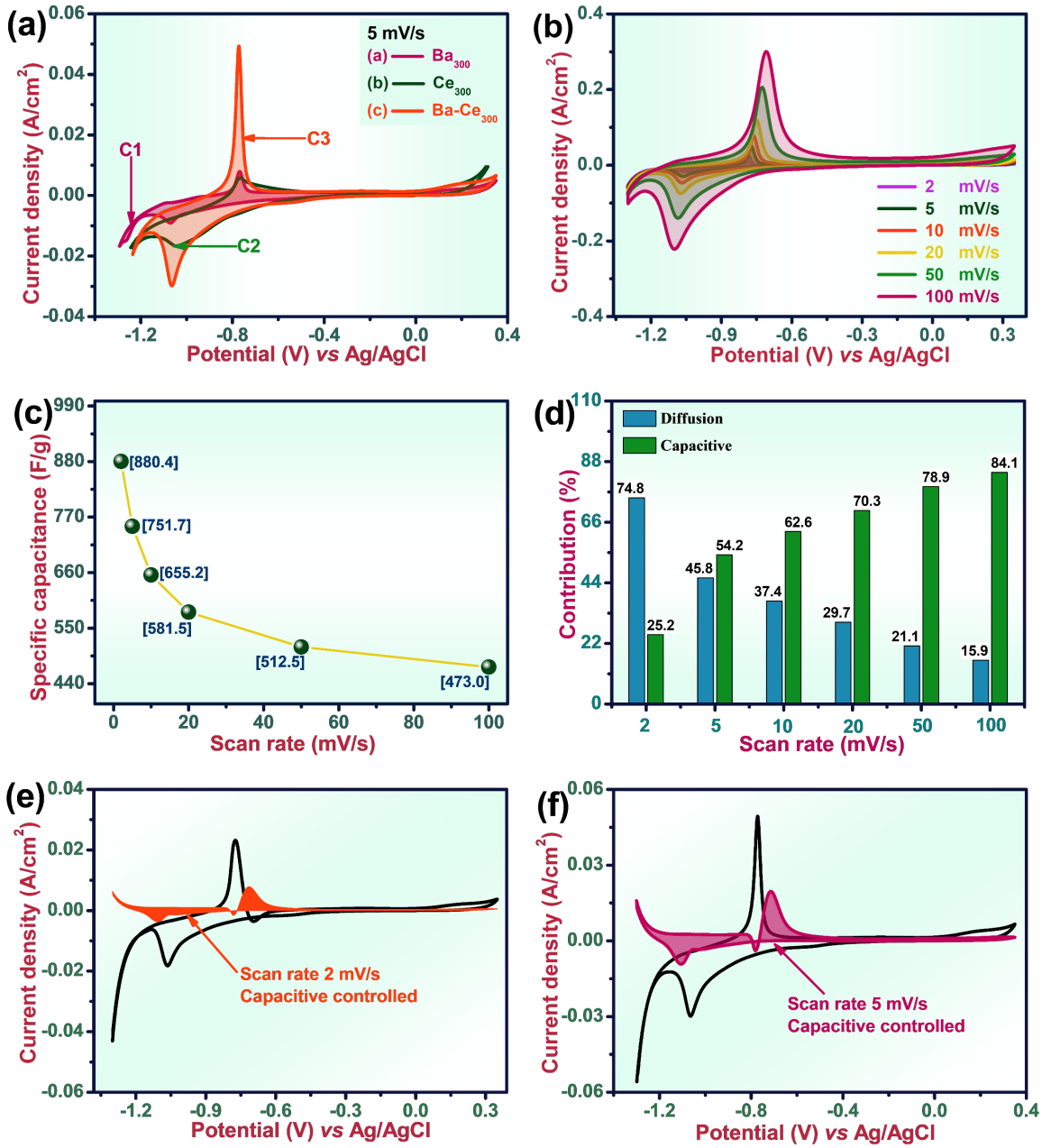


Fig 6: (a) The CV of electrode Ba_{300}, Ce_{300}, and Ba-Ce_{300} at scan rate of 5 mV/s in 1M KOH

electrolyte, (b) CV plots of electrode Ba-Ce_{300} at dissimilar sweep rates from 2-100 mV/s, (c) Region plot of electrode Ba-Ce_{300} SC in F/g Vs sweep rate in mV/s, (d) The percentage of capacitive and diffusion charges collected against numerous sweep rates, A separation of diffusion current from a total CV pattern at a scan rate of (e) 2 mV/s and (f) 100 mV/s of the electrode Ba-Ce_{300}.

3.5.2 Chronopotentiometry (CP) study

To further investigate the performance and analyze the relationship between the Ba-Ce_{300} electrodes, chronopotentiometry (CP) measurements were performed in 1M KOH at various current densities. At a current density of 6 mA/cm², as revealed in **Fig. 7 (a)**, a Ba-Ce_{300} electrode exhibited the longest discharge time, suggesting that the BaO-CeO_2 mixed-phase nanocomposite is more efficient than the individual BaO and CeO_2 materials. The **Fig. 7 (b)** presents the CP curves for the Ba-Ce_{300} electrode at dissimilar current densities ranging from 3-7 mA/cm². This behavior highlights the superior performance of the Ba-Ce_{300} electrode, which benefits from the crinum asiaticum flower-like morphology that enhances electron transfer, increases the surface area, and reduces the resistance for ion penetration. Cycling stability, an essential factor for practical supercapacitor applications, was also assessed. The specific capacitance (SC) of the Ba-Ce_{300} electrodes, shown in **Fig. 7 (c)**, was measured over multiple cycles at the sweep rate of 100 mV/s. A SC of an optimized BaO-CeO_2 electrode gradually decreased after the first 1,500 cycles. However, after 6,500 cycles, the Ba-Ce_{300} electrodes retained 97 % of their initial capacitance, showcasing the excellent long-term stability of the BaO-CeO_2 composite. A comparison of a cyclic permanency of Ba-Ce_{300} with previously reported cerium and barium-based metal oxide electrodes is presented in **Table 1** [11,12,74–77,13,16–19,21,22,73], further underscoring the promising performance of the BaO-CeO_2 nanocomposite.

3.5.3 Electrochemical impedance spectroscopy study

The electrochemical impedance spectroscopy (EIS) measurements were performed on the Ba-Ce_{300} electrode at an open-circuit potential (OCP) of -0.9472 V in 1M KOH over a frequency range of 1 mHz to 1 MHz to evaluate its internal resistance and capacitive behavior, as depicted in the Nyquist plot (**Fig. 7d**). The plot consists of three distinct regions: the high-frequency region exhibits a charge transfer resistance (Rct) associated with Faradaic reactions, while the low-frequency region demonstrates pseudocapacitive behavior, contributing to the depressed semicircle. The internal resistance (Ri) was calculated as 0.97 Ω. The knee frequency, where the semicircle deviates, indicates the transition point where capacitive performance dominates [3]. The inset of **Fig. 7(d)** presents the experimental and simulated data obtained using ZsimpWin software, along with the equivalent circuit model [20]. The key parameters derived from the fitting include R_s = 0.9 Ω, R_{ct} = 495 Ω, R_L = 0.7 Ω, CPE1 = 44 × 10^{-4} F, CPE2 = 3 × 10^{-5} F, and a Warburg element (W) of 1.1 F.

The further analysis of the Ba-Ce_{300} electrode impedance behavior is shown in **Fig. (S2),** which presents the Bode plot obtained at OCP of -0.9 V at 5 mA in 1M KOH. The phase angle at lower frequencies stabilizes around -65.2°, suggesting that the electrode exhibits nearly supercapacitive characteristics, as the ideal phase angle for supercapacitors is -90°. The phase angle and impedance response are indicative of a capacitor-like behavior, where the capacitive and resistive elements show similar features. By applying the relaxation time constant formula ($\tau_0 = 1/f_0$), the shorter relaxation time of the Ba-Ce_{300} electrode (1.2 ms) suggests efficient diffusion of electrolyte ions at an electrode and electrolyte interface, facilitating rapid charge and discharge processes. This rapid ion diffusion contributes to an enhanced supercapacitive presentation of an electrode [71,78].

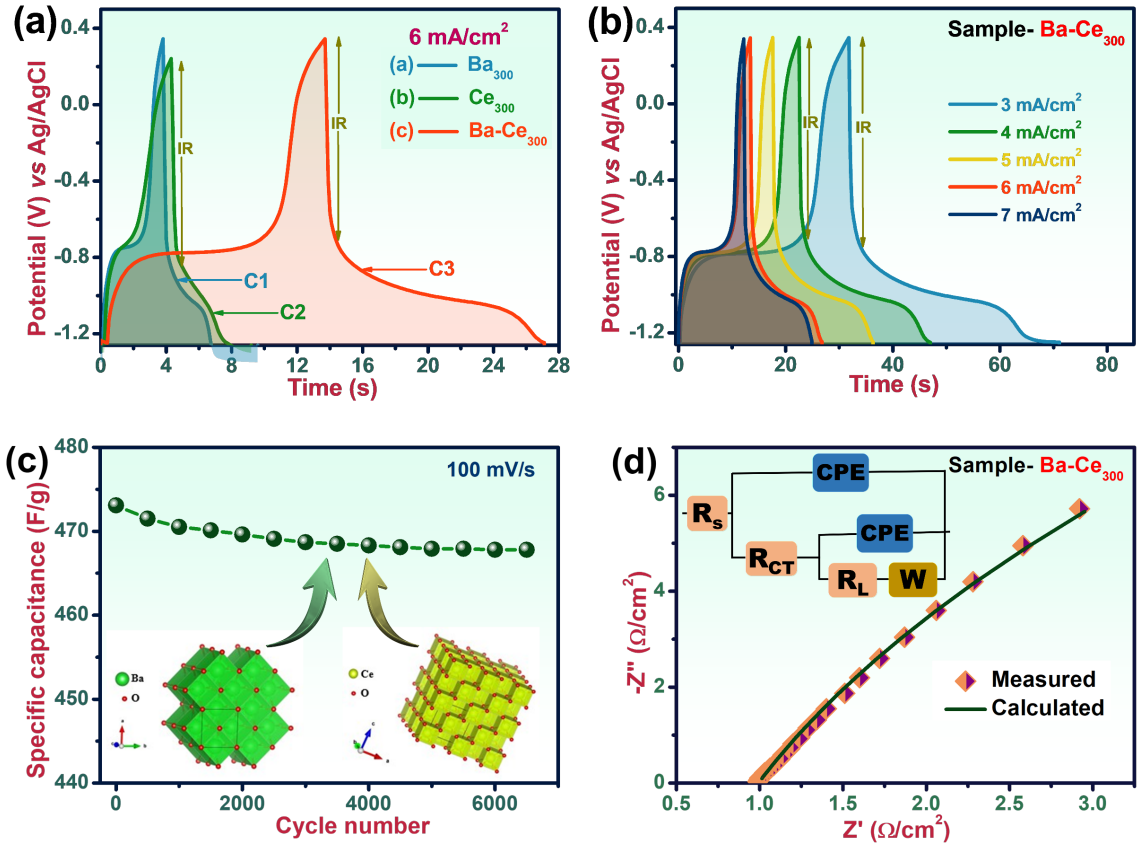


Fig. 7: (a) Chronopotentiometric curves of electrode Ba_{300}, Ce_{300} and Ba-Ce_{300} at current density of 6 mA/cm^2 in 1M KOH electrolyte, (b) Chronopotentiometric curves of electrode Ba-Ce_{300} at different current density in mA/cm^2, (c) Cycling stability test at a constant scan rate of 100 mV/s of Ba-Ce_{300} electrode, (d) Nyquist plots of electrode Ba-Ce_{300}.

3.6 BaO-CeO_2//Activated carbon (AC) asymmetric supercapacitor device analysis

The BaO-CeO_2//AC ASSD device has assembled using PVA-KOH gel as a separator, BaO-CeO_2 as a positive electrode, as well activated carbon (AC) as an negative electrode. **Fig. 8 (a)** presents a CV curves for aa BaO-CeO_2 and AC electrodes in a 1 M KOH aqueous solution. The AC electrode displayed a near-rectangular CV curve, characteristic of typical electric double-layer capacitance (EDLC) behavior, and was operated within the potential window of -1.9 to -1.2 V. In contrast, the BaO-CeO_2 electrode, operating within the potential window of -1.3 to 0.4 V at a

sweep rate of 2 mV/s, exhibited two distinct redox peaks. These peaks, indicative of the pseudocapacitance performance of BaO-CeO_2, arise from the faradaic redox reactions at an electrode and electrolyte boundary. The anodic peak corresponds to oxidation, while the cathodic peak is associated with the reverse reaction. This suggests that the capacitance observed for BaO-CeO_2 is primarily attributed to pseudocapacitance rather than the EDLC mechanism seen in the AC electrode.

The **Fig. 8 (b)** displays a CV plots of a BaO-CeO_2//AC cell at varying sweep rates from 5-100 mV/s, measured within a potential window of -1.8 to 0.4 V. The redox peaks observed across all scan rates confirm the redox processes occurring at the interface among a positive BaO-CeO_2 as well negative AC electrodes, with a 1 M KOH gel electrolyte facilitating these reactions [2]. The specific capacitance (SC) values obtained at 5, 10, 20, 50, and 100 mV/s were 213, 194, 149, 111, and 89 F/g, correspondingly, as revealed in **Fig. 8 (c)**. These results were compared with previously reported performances of other AC based asymmetric supercapacitor devices, as summarized in **Table 2** [2,79–86]. The BaO-CeO_2 composite electrode (Ba-Ce_{300}) demonstrated excellent performance, positioning it as a strong candidate for use as a positive electrode in high-performance energy storing applications. The persistence of the redox peaks at higher scan rates (up to 100 mV/s) indicates a robust rate capability of the BaO-CeO_2//AC ASSD device, confirming its potential for high-rate applications in energy storage systems.

The charge-discharge (CP) curves collected at numerous current densities ranging from 2 to 6 mA/cm^2 exhibited similar trends, as depicted in **Fig. 8 (d)**, for the asymmetric BaO-CeO_2//AC supercapacitor. The high conductivity of the BaO-CeO_2//AC ASSD device contributed significantly to its excellent performance, with the graph indicating minimal voltage (IR) losses, which is an indicator of efficient charge/discharge processes. The SE as well SP values at different

current densities, shown in **Fig. 8 (e)**, were 17.8, 14.8, 13.6, 13.0, and 12.8 Wh/kg for SE, and 1.3, 1.9, 2.5, 3.1, and 3.8 kW/kg for SP, respectively. These values demonstrate the excellent balance between energy storage and power delivery in the device. The stability of the BaO-CeO_2//AC device was assessed, with the curve shown in **Fig. 8 (f)**, confirming the device robustness over multiple charge-discharge cycles. The combination of high energy storage, power density, and excellent stability makes the BaO-CeO_2//AC asymmetric supercapacitor an favorable candidate for energy storing applications.

The long-term cycling concert a the BaO-CeO_2//Activated Carbon ASSD device has assessed over 5,500 cycles at a sweep rate of 100 mV/s within a 2.38 V voltage range. The device exhibited remarkable stability, retaining 98 % of its capacitance after the full 5,500 cycles, as shown in **Fig. 8 (g)**. The Nyquist plot for the ASSD revealed an internal resistance of 1.6 **Ω**, confirming the efficient electrochemical behavior of the device. A Bode plot, shown in **Fig. (S3)**, was used to explore the relationship between the impedance phase angle and frequency, revealing a phase angle of -56.1º, which is relatively close to the ideal value of -90º for a pure capacitor. At higher frequencies, the phase angle is reduced due to resistive components in the system, but the close proximity to -90º indicates a predominantly capacitive nature. The capacitive response frequency (f_0) for the device was determined from the Bode plot at a phase angle of -45º, yielding a frequency of 656 Hz. This was then used to calculate a reaction time ($\tau_0 = 1/f_0$) of 1.5 ms, demonstrating the device quick response to charge/discharge cycles. In practical demonstrations, two fully charged BaO-CeO_2//AC devices powered a green LED for 8 to 10 minutes, as shown in **Fig. 8 (h)**, highlighting their impressive energy density. These results emphasize the great potential of the BaO-CeO_2//Activated Carbon ASSD in energy storage applications, especially for powering portable electronic devices. The device high cycling stability, fast charge/discharge kinetics, and

substantial energy density make it an ideal candidate for future energy storage technologies.

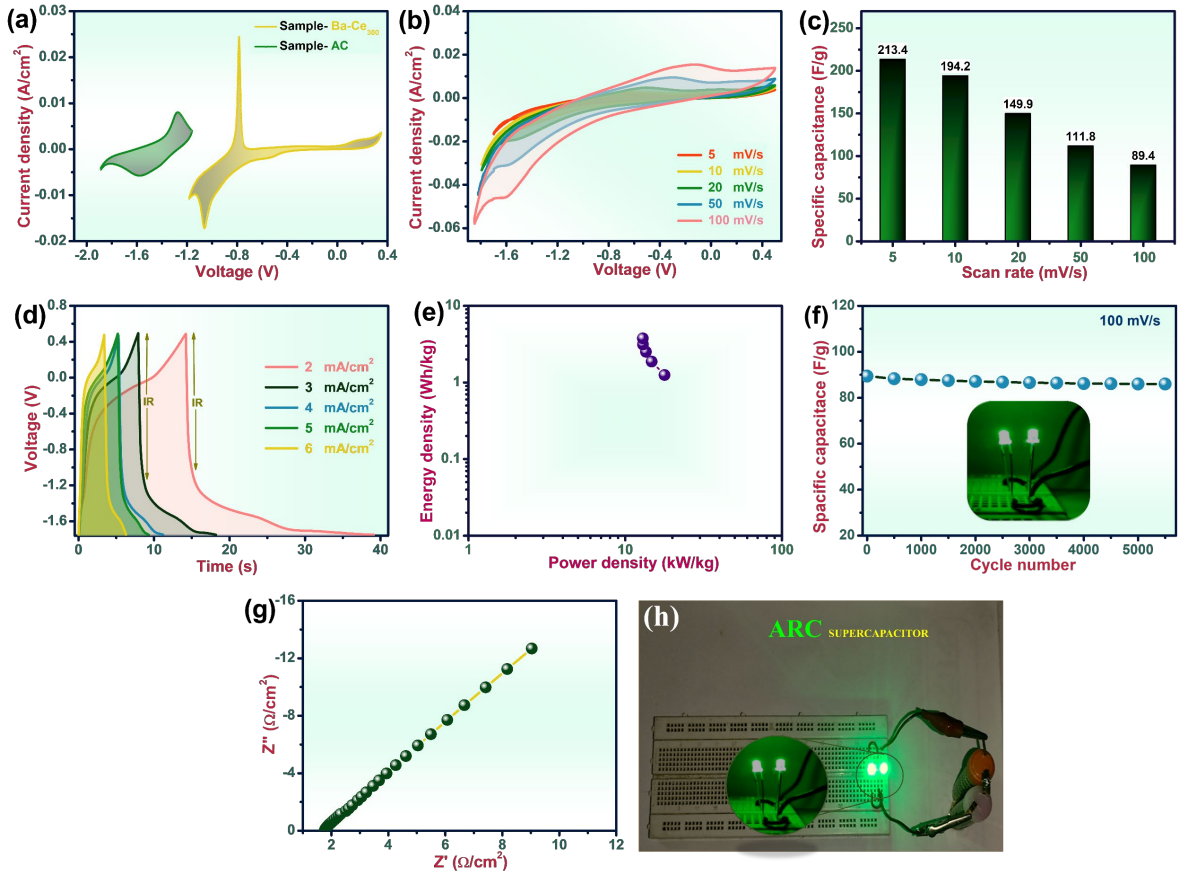


Fig 8: (a) CV plots of an individual electrodes at 2 mV/s in 1M KOH electrolyte at dissimilar applied voltage, confirming a possibility of manufacturing the asymmetric device, (b) CV plots of BaO-CeO_2//AC ASSD device at the sweep rate of 2 to 100 mV/s, (c) Variation of a specific capacitance as a function of dissimilar sweep rate in mV/s, (d) Chronopotentiometric plots of BaO-CeO_2//AC ASSD device at dissimilar current densities, (e) Ragone plot of BaO-CeO_2//AC ASSD device, (f) The plot of capacitance retention through cycle number of BaO-CeO_2//AC ASSD device, (g) The Nyquist plot of BaO-CeO_2//AC ASSD, (h) The photograph shows the glow of green LED using BaO-CeO_2//AC ASSD device.

Conclusion

In summary, the SILAR method was employed to synthesize a BaO-CeO_2 mixed-phase

nanocomposite resembling the structure of crinum asiaticum flowers. These nanocomposites demonstrated excellent electrochemical stability, achieving a high SC of 880 F/g at a scan rate of 2 mV/s, along with impressive capacitance retention of 97 % after 6,500 cycles at 100 mV/s. Furthermore, the BaO-CeO_2//AC ASSD exhibited a specific capacitance (SC) of 213 F/g at 2 mV/s, with remarkable cycling stability, retaining 98 % of its initial capacitance after 5500 cycles. The device also showcased outstanding energy density (17.8 Wh/kg at 6.8 kW/kg). In practical applications, two fully charged devices powered green LED for 8 to 10 minutes, demonstrating the device substantial potential as an energy storage solution. This work highlights that the synergy between conductive polymers and transition metal oxides not only enhances capacitance but also leverages the high surface area of the materials and their robust electrochemical properties, making BaO-CeO_2 mixed-phase nanocomposites promising candidates for real-world supercapacitor applications.

CRediT authorship contribution statement

Rushikesh G. Bobade: Conceptualization, Methodology, Software, Investigation, Data Curation, Writing - Original Draft, Visualization. **Akhil P. Khedulkar :** Conceptualization, Software, Formal analysis. **Shoyebmohamad F. Shaikh:** Formal analysis, Resources, Writing - Review & Editing, Supervision. **Vijay S. Raykar:** Software, Validation, Formal analysis. **Bidhan Pandit:** Validation, Formal analysis, Writing - Review & Editing, Supervision. **Pradip B. Sarawade:** Formal analysis, Investigation, Writing - Review & Editing. **Revanappa C. Ambare:** Conceptualization, Writing - Review & Editing, Visualization, Supervision.

Institutional Review Board Statement: Not applicable.

Informed Consent Statement: Not applicable.

Data Availability Statement: Data will be made available on request.

Conflicts of Interest: The authors declare that they have no known competing financial interests or personal relationships that could have appeared to influence the work reported in this paper.

Acknowledgments

Author Dr. R. C. Ambare expresses gratitude to Prof. (Dr.) B.J. Lokhande for supplying the electrochemical characterizations. The authors extend their sincere appreciation to the Researchers Supporting Project number (RSP2024R370), King Saud University, Riyadh, Saudi Arabia for the financial support. Bidhan Pandit acknowledges the Iberdrola Foundation under the Marie Skłodowska-Curie Grant Agreement No 101034297. Chun Huang acknowledges funding from the ERC Starting Grant (EP/Y009908/1), and research projects (EP/X52556X/1, FIRG060, FIRG066).

References

[1] J. Zhang, F. Liu, J.P. Cheng, X.B. Zhang, Binary Nickel–Cobalt Oxides Electrode Materials for High-Performance Supercapacitors: Influence of its Composition and Porous Nature, ACS Appl. Mater. Interfaces 7 (2015) 17630–17640. https://doi.org/10.1021/acsami.5b04463.

[2] R.G. Bobade, U.T. Nakate, P. Roasiah, M. Ouladsmane, B.J. Lokhande, R.C. Ambare, Nanoarchitectonics of Bi2CuO4 electrodes for asymmetric Bi2CuO4//AC solid-state device in supercapacitor application, Inorg. Chem. Commun. 154 (2023) 110998. https://doi.org/10.1016/j.inoche.2023.110998.

[3] R.G. Bobade, N.B. Dabke, S.F. Shaikh, B.J. Lokhande, R.S. Mane, R.C. Ambare, Facile chemical synthesis of BaO:MgO nanorods for designing distinctive solid-state asymmetric supercapacitor device with activated carbon, J. Energy Storage 84 (2024) 110776. https://doi.org/10.1016/j.est.2024.110776.

[4] R.G. Bobade, N.B. Dabke, S.F. Shaikh, A.M. Al-Enizi, B. Pandit, B.J. Lokhande, R.C. Ambare, Concentration-dependent SILAR synthesized Di-bismuth copper oxide nano-materials electrode in asymmetric supercapacitor, J. Mater. Sci. Mater. Electron. 35 (2024) 129. https://doi.org/10.1007/s10854-023-11818-4.

[5] Q. Chu, W. Wang, X. Wang, B. Yang, X. Liu, J. Chen, Hierarchical NiCo2O4@nickel-sulfide nanoplate arrays for high-performance supercapacitors, J. Power Sources 276 (2015) 19–25. https://doi.org/10.1016/j.jpowsour.2014.11.015.

[6] R.G. Bobade, N.B. Dabke, S.F. Shaikh, A.M. Al-Enizi, B. Pandit, B.J. Lokhande, R.C. Ambare, Influence of Deposition Potential on Electrodeposited Bismuth–Copper Oxide Electrodes for Asymmetric Supercapacitor, Batter. Supercaps 7 (2024). https://doi.org/10.1002/batt.202400163.

[7] D.S. Gaikwad, R.G. Bobade, U.T. Nakate, P. Rosaiah, A.M. Tighezza, B.J. Lokhande, R.C. Ambare, SILAR-synthesized Co3O4/Bi2O3 on copper substrate nanocomposite electrode and asymmetric Co3O4/Bi2O3/CuO: AC solid-state device in supercapacitor, J. Mater. Sci. Mater. Electron. 35 (2024) 489. https://doi.org/10.1007/s10854-024-12220-4.

[8] S.G. Randive, R.G. Bobade, R.C. Ambare, B.J. Lokhande, Spray pyrolyzed thorn-like nanostructured nickel oxide electrodes for symmetric supercapacitor device, J. Mater. Sci. Mater. Electron. 35 (2024) 577. https://doi.org/10.1007/s10854-024-12229-9.

[9] D.S. Gaikwad, R.G. Bobade, V.B. Suryawanshi, U.T. Nakate, S.F. Shaikh, A.M. Al-Enizi, N.B. Dabke, B.J. Lokhande, R.C. Ambare, Electrochemical property of nanosphere-like MgO electrode synthesized via SILAR in asymmetric supercapacitor, J. Mater. Sci. Mater. Electron. 35 (2024) 363. https://doi.org/10.1007/s10854-024-12196-1.

[10] V.B. Suryawanshi, R.G. Bobade, D.S. Gaikwad, U.T. Nakate, S.F. Shaikh, B.J. Lokhande, R.C. Ambare, Nano-architectured BaO thin film electrode synthesized via SILAR technique for supercapacitor application, Chem. Pap. 78 (2024) 4689–4697. https://doi.org/10.1007/s11696-024-03400-x.

[11] M. Sadeghinia, J.S. Shayeh, F. Fatemi, M. Rahmandoust, A. Ehsani, M. Rezaei, Electrochemical study of perlite-barium ferrite/conductive polymer nano composite for super capacitor applications, Int. J. Hydrogen Energy 44 (2019) 28088–28095. https://doi.org/10.1016/j.ijhydene.2019.09.085.

[12] B. Padmadevi, A. Pugazhendhi, A.S. Khalifa, R. Shanmuganathan, T. Kalaivani, Novel MnO2-CuO-BaO metal oxide nanocomposite for high performance supercapacitors, Process Biochem. 110 (2021) 176–180. https://doi.org/10.1016/j.procbio.2021.08.017.

[13] M. Shanmugavadivel, V.V. Dhayabaran, M. Subramanian, Nanosized BaMnO3 as high performance supercapacitor electrode material: Fabrication and characterization, Mater.

Lett. 181 (2016) 335–339. https://doi.org/10.1016/j.matlet.2016.05.135.

[14] S. Utara, S. Hunpratub, S. Pinitsoontorn, S. Phokha, Characterization and magnetic performance of pure CeO2 nanoparticles via an ozonolysis reaction, Results Phys. (2021). https://doi.org/10.1016/j.rinp.2021.104890.

[15] S.H. Ahmed, M. Bakiro, F.I.A. Aljasmi, A.M.O. Albreiki, S. Bayane, A. Alzamly, Investigation of the band gap and photocatalytic properties of CeO2/rGO composites, Mol. Catal. (2020). https://doi.org/10.1016/j.mcat.2020.110874.

[16] K. Prasanna, P. Santhoshkumar, Y.N. Jo, I.N. Sivagami, S.H. Kang, Y.C. Joe, C.W. Lee, Highly porous CeO2 nanostructures prepared via combustion synthesis for supercapacitor applications, Appl. Surf. Sci. 449 (2018) 454–460. https://doi.org/10.1016/j.apsusc.2017.12.130.

[17] G.P. Ojha, B. Pant, S.J. Park, M. Park, H.Y. Kim, Synthesis and characterization of reduced graphene oxide decorated with CeO2-doped MnO2 nanorods for supercapacitor applications, J. Colloid Interface Sci. (2017). https://doi.org/10.1016/j.jcis.2017.01.100.

[18] M. Mazloum-Ardakani, F. Sabaghian, M. Yavari, A. Ebady, N. Sahraie, Enhance the performance of iron oxide nanoparticles in supercapacitor applications through internal contact of α-Fe2O3@CeO2 core-shell, J. Alloys Compd. (2020). https://doi.org/10.1016/j.jallcom.2019.152949.

[19] N. Chakrabarty, A. Dey, S. Krishnamurthy, A.K. Chakraborty, CeO2/Ce2O3 quantum dot decorated reduced graphene oxide nanohybrid as electrode for supercapacitor, Appl. Surf. Sci. (2021). https://doi.org/10.1016/j.apsusc.2020.147960.

[20] S.S. Pujari, R.G. Bobade, S.F. Shaikh, A.M. Al-Enizi, R.C. Ambare, B.J. Lokhande, A binderless Ru:α-Fe2O3 binary nanocomposite electrode for supercapacitor applications, J. Mater. Sci. Mater. Electron. 35 (2024) 2162. https://doi.org/10.1007/s10854-024-13857-x.

[21] M. Vanitha, Keerthi, P. Cao, N. Balasubramanian, Ag nanocrystals anchored CeO2/graphene nanocomposite for enhanced supercapacitor applications, J. Alloys Compd. 644 (2015) 534–544. https://doi.org/10.1016/j.jallcom.2015.03.221.

[22] A. Jeyaranjan, T.S. Sakthivel, C.J. Neal, S. Seal, Scalable ternary hierarchical microspheres composed of PANI/ rGO/CeO2 for high performance supercapacitor applications, Carbon N. Y. (2019). https://doi.org/10.1016/j.carbon.2019.05.043.

[23] R. Pitcheri, S.P. Mooni, D. Radhalayam, M. Nora, S. Roy, F.A.M. Al-Zahrani, M. Suneetha,

Effect of Ce-doping on the structural, morphological, and electrochemical features of Co3O4 nanoparticles synthesized by solution combustion method for battery-type supercapacitors, Ceram. Int. 50 (2024) 50504–50515. https://doi.org/10.1016/j.ceramint.2024.09.396.

[24] R. Silambarasan, U.S.S.S. Perisetti, A. Ramesh, K. Anbalagan, UV Light-Driven Photocatalytic Performance of CeO 2 and Co Ion-Doped CeO 2 Nanoparticles: High-Efficiency Electrochemical and Chromaticity Blue LED Application, ChemistrySelect 9 (2024). https://doi.org/10.1002/slct.202402609.

[25] H.S. Lalithamba, G.K. Prashanth, H.K.E. Latha, Rashmi, A. Siddekha, G. Nagendra, Cerium oxide nanoparticles: sustainable synthesis and diverse applications in electrical properties, catalysis and biomedicine, Chem. Pap. 79 (2025) 193–209. https://doi.org/10.1007/s11696-024-03770-2.

[26] S. Jafari, Z. Shaghaghi, Engineering active sites in ternary CeO2-CuO-Mn3O4 heterointerface embedded in reduced graphene oxide for boosting water splitting activity, Sci. Rep. 15 (2025) 4145. https://doi.org/10.1038/s41598-025-87423-8.

[27] I.T. Bello, K.O. Otun, G. Nyongombe, O. Adedokun, G.L. Kabongo, M.S. Dhlamini, Synthesis, Characterization, and Supercapacitor Performance of a Mixed-Phase Mn-Doped MoS2 Nanoflower, Nanomaterials (2022). https://doi.org/10.3390/nano12030490.

[28] I. Khan, S.S. Shah, A.H. Hendi, M. Ashraf, Y. Cho, S. Ali, S. Wooh, Tailoring performance of hybrid supercapacitors by fluorine-rich block copolymer-derived carbon coated mixed-phase TiO2 nanoparticles, J. Alloys Compd. (2023). https://doi.org/10.1016/j.jallcom.2023.172175.

[29] P. Kour, Deeksha, S. Kour, A.L. Sharma, K. Yadav, Mixed-phase MoS2 nanosheets anchored carbon nanofibers for high energy symmetric supercapacitors, J. Energy Storage (2023). https://doi.org/10.1016/j.est.2023.107054.

[30] Y. Mao, J. Xie, C. Guo, H. Liu, H. Xiao, W. Hu, Simultaneously high mass-loading and volumetric energy density in Ag2O-intercalated MnO2-based supercapacitor with rapid electron/ion transport channels, Chem. Eng. J. (2021). https://doi.org/10.1016/j.cej.2021.131188.

[31] Y. Gao, S. Zhang, X. Li, L. Li, L. Bao, N. Zhang, J. Peng, X. Li, Synergistically optimizing electronic structure and reducing ions transport resistance by oxygen functional groups and

defects in carbon for superior sodium capture and potassium storage capability, Carbon N. Y. (2021). https://doi.org/10.1016/j.carbon.2021.05.039.

[32] J. Wu, Understanding the Electric Double-Layer Structure, Capacitance, and Charging Dynamics, Chem. Rev. (2022). https://doi.org/10.1021/acs.chemrev.2c00097.

[33] B.E. Conway, V. Birss, J. Wojtowicz, The role and utilization of pseudocapacitance for energy storage by supercapacitors, J. Power Sources (1997). https://doi.org/10.1016/S0378-7753(96)02474-3.

[34] A.G. Olabi, Q. Abbas, A. Al Makky, M.A. Abdelkareem, Supercapacitors as next generation energy storage devices: Properties and applications, Energy (2022). https://doi.org/10.1016/j.energy.2022.123617.

[35] G. Rani, Bhawna, R. Ahlawat, A critical examination of polyaniline and its composite materials: Augmenting supercapacitor performance and diversifying application potential, J. Energy Storage 97 (2024) 112690. https://doi.org/10.1016/j.est.2024.112690.

[36] S.S. Shah, F. Niaz, M.A. Ehsan, H.T. Das, M. Younas, A.S. Khan, H.U. Rahman, S.M.A. Nayem, M. Oyama, M.A. Aziz, Advanced strategies in electrode engineering and nanomaterial modifications for supercapacitor performance enhancement: A comprehensive review, J. Energy Storage 79 (2024) 110152. https://doi.org/10.1016/j.est.2023.110152.

[37] E. Dhandapani, S. Thangarasu, S. Ramesh, K. Ramesh, R. Vasudevan, N. Duraisamy, Recent development and prospective of carbonaceous material, conducting polymer and their composite electrode materials for supercapacitor — A review, J. Energy Storage 52 (2022) 104937. https://doi.org/10.1016/j.est.2022.104937.

[38] S.S. Pujari, R.G. Bobade, R.C. Ambare, B.J. Lokhande, Temperature-Contingent Electrochemical Capacitive Concert of Nanospheres Fe2O3 as a Supercapacitor Electrode, ES Chem. Sustain. (2024). https://doi.org/10.30919/escs1323.

[39] S.S. Pujari, R.G. Bobade, R.C. Ambare, B.J. Lokhande, Facile Fabrication of Binary Mixed Phase Ru Doped Fe2O3 as a Potential Electrode Material for High-Performance Supercapacitors, ES Energy Environ. (2024). https://doi.org/10.30919/esee1324.

[40] S.G. Deshmukh, V. Kheraj, K.J. Karande, S.G. Kulkarni, eds., Thin Film Nanomaterials: Synthesis, Properties and Innovative Energy Applications, BENTHAM SCIENCE PUBLISHERS, 2024. https://doi.org/10.2174/9789815256086124010l.

[41] B.R. Sankapal, H.B. Gajare, S.S. Karade, D.P. Dubal, Anchoring cobalt oxide nanoparticles on to the surface multiwalled carbon nanotubes for improved supercapacitive performances, RSC Adv. 5 (2015) 48426–48432. https://doi.org/10.1039/C5RA06377A.

[42] B.E. Treml, B.H. Savitzky, A.M. Tirmzi, J.C. Dasilva, L.F. Kourkoutis, T. Hanrath, Successive Ionic Layer Absorption and Reaction for Postassembly Control over Inorganic Interdot Bonds in Long-Range Ordered Nanocrystal Films, ACS Appl. Mater. Interfaces (2017). https://doi.org/10.1021/acsami.7b01588.

[43] S.S. Raut, B.R. Sankapal, Comparative studies on MWCNTs, Fe2O3 and Fe2O3/MWCNTs thin films towards supercapacitor application, New J. Chem. (2016). https://doi.org/10.1039/c5nj03628c.

[44] B.R. Sankapal, A. Ennaoui, T. Guminskaya, T. Dittrich, W. Bohne, J. Röhrich, E. Strub, M.C. Lux-Steiner, Characterization of p-CuI prepared by the SILAR technique on Cu-tape/n-CuInS2 for solar cells, Thin Solid Films 480–481 (2005) 142–146. https://doi.org/10.1016/j.tsf.2004.11.020.

[45] B.R. Sankapal, C.D. Lokhande, Photoelectrochemical characterization of Bi2Se3 thin films deposited by SILAR technique, Mater. Chem. Phys. (2002). https://doi.org/10.1016/S0254-0584(01)00362-5.

[46] S.P. Ratnayake, J. Ren, E. Colusso, M. Guglielmi, A. Martucci, E. Della Gaspera, SILAR Deposition of Metal Oxide Nanostructured Films, Small (2021). https://doi.org/10.1002/smll.202101666.

[47] H.. Pathan, B.. Sankapal, J.. Desai, C.. Lokhande, Preparation and characterization of nanocrystalline CdSe thin films deposited by SILAR method, Mater. Chem. Phys. 78 (2003) 11–14. https://doi.org/10.1016/S0254-0584(02)00198-0.

[48] A.P. Khedulkar, B. Pandit, W.-J. Yu, R. Doong, Urchin-like Ni Co hydroxide@tamarind seed biochar for high performance supercapacitor, J. Energy Storage 84 (2024) 110639. https://doi.org/10.1016/j.est.2024.110639.

[49] B. Pandit, E.S. Goda, M. Ubaidullah, S.F. Shaikh, U.T. Nakate, A.P. Khedulkar, A. ul H.S. Rana, D. Kumar, R. Doong, Hexagonal δ-MnO2 nanoplates as efficient cathode material for potassium-ion batteries, Ceram. Int. 48 (2022) 28856–28863. https://doi.org/10.1016/j.ceramint.2022.03.279.

[50] A.P. Khedulkar, B. Pandit, W.J. Yu, R. an Doong, Urchin-like Ni[sbnd]Co hydroxide@

tamarind seed biochar for high performance supercapacitor, J. Energy Storage (2024). https://doi.org/10.1016/j.est.2024.110639.

[51] C.C. Wei, P.H. Lin, C.E. Hsu, W. Bin Jian, Y.L. Lin, J.T. Chen, S. Banerjee, C.W. Chu, A.P. Khedulkar, R.A. Doong, K. Tsukagoshi, Boosting areal capacitance in WO3-based supercapacitor materials by stacking nanoporous composite films, Cell Reports Phys. Sci. (2024). https://doi.org/10.1016/j.xcrp.2024.101836.

[52] B. Pandit, B.R. Sankapal, Cerium Selenide Nanopebble/Multiwalled Carbon Nanotube Composite Electrodes for Solid-State Symmetric Supercapacitors, ACS Appl. Nano Mater. 5 (2022) 3007–3017. https://doi.org/10.1021/acsanm.2c00374.

[53] P. Giannozzi, S. Baroni, N. Bonini, M. Calandra, R. Car, C. Cavazzoni, D. Ceresoli, G.L. Chiarotti, M. Cococcioni, I. Dabo, A. Dal Corso, S. De Gironcoli, S. Fabris, G. Fratesi, R. Gebauer, U. Gerstmann, C. Gougoussis, A. Kokalj, M. Lazzeri, L. Martin-Samos, N. Marzari, F. Mauri, R. Mazzarello, S. Paolini, A. Pasquarello, L. Paulatto, C. Sbraccia, S. Scandolo, G. Sclauzero, A.P. Seitsonen, A. Smogunov, P. Umari, R.M. Wentzcovitch, QUANTUM ESPRESSO: A modular and open-source software project for quantum simulations of materials, J. Phys. Condens. Matter 21 (2009) 395502. https://doi.org/10.1088/0953-8984/21/39/395502.

[54] M.A. Ansari, N. Jahan, Structural and Optical Properties of BaO Nanoparticles Synthesized by Facile Co-precipitation Method, Mater. Highlights 2 (2021) 23. https://doi.org/10.2991/mathi.k.210226.001.

[55] A. Toghan, M. Khairy, E.M. Kamar, M.A. Mousa, Effect of particle size and morphological structure on the physical properties of NiFe2O4 for supercapacitor application, J. Mater. Res. Technol. (2022). https://doi.org/10.1016/j.jmrt.2022.06.095.

[56] K. Seevakan, A. Manikandan, P. Devendran, A. Shameem, T. Alagesan, Microwave combustion synthesis, magneto-optical and electrochemical properties of NiMoO4 nanoparticles for supercapacitor application, Ceram. Int. (2018). https://doi.org/10.1016/j.ceramint.2018.04.235.

[57] R. Kumar, P.S. Shukla, G.D. Varma, M. Bag, Synthesis of porous electrode from CH3NH3PbBr3 single crystal for efficient supercapacitor application: Role of morphology on the charge storage and stability, Electrochim. Acta 398 (2021) 139344. https://doi.org/10.1016/j.electacta.2021.139344.

[58] D. Anbuselvan, G. Anitha, S. Nilavazhagan, L.B. Chandrasekar, M. Karunakaran, K. Sakthipandi, Electrochemical investigations of Mn-doped ZnO/rGO nanoparticles electrode material for supercapacitor application and its enhanced antimicrobial activity, Eur. Phys. J. Plus 139 (2024) 1054. https://doi.org/10.1140/epjp/s13360-024-05856-y.

[59] P. Burroughs, A. Hamnett, A.F. Orchard, G. Thornton, Satellite structure in the X-ray photoelectron spectra of some binary and mixed oxides of lanthanum and cerium, J. Chem. Soc. Dalt. Trans. (1976). https://doi.org/10.1039/DT9760001686.

[60] V. Stetsovych, F. Pagliuca, F. Dvořák, T. Duchoň, M. Vorokhta, M. Aulická, J. Lachnitt, S. Schernich, I. Matolínová, K. Veltruská, T. Skála, D. Mazur, J. Mysliveček, J. Libuda, V. Matolín, Epitaxial Cubic Ce 2 O 3 Films via Ce–CeO 2 Interfacial Reaction, J. Phys. Chem. Lett. 4 (2013) 866–871. https://doi.org/10.1021/jz400187j.

[61] T. Ghoshal, P.G. Fleming, J.D. Holmes, M.A. Morris, The stability of "Ce2O3" nanodots in ambient conditions: a study using block copolymer templated structures, J. Mater. Chem. 22 (2012) 22949. https://doi.org/10.1039/c2jm35073d.

[62] E. Paparazzo, Use and mis-use of x-ray photoemission spectroscopy Ce3d spectra of Ce 2 O 3 and CeO 2, J. Phys. Condens. Matter 30 (2018) 343003. https://doi.org/10.1088/1361-648X/aad248.

[63] M. Ye, T. Su, J. Li, X. Chen, D. Ying, S. Wu, Z. Wang, N. Duan, Multifunctional Ce-MOF@PdNPs with colorimetric fluorescent electrochemical activity for ultrasensitive and accurate detection of diethylstilbestrol, Nano Res. 17 (2024) 9990–9998. https://doi.org/10.1007/s12274-024-6951-4.

[64] S.M. AlShehri, J. Ahmed, T. Ahamad, B.M. Almaswari, A. Khan, Efficient photodegradation of methylthioninium chloride dye in aqueous using barium tungstate nanoparticles, J. Nanoparticle Res. 19 (2017) 289. https://doi.org/10.1007/s11051-017-3970-z.

[65] V. Stetsovych, F. Pagliuca, F. Dvořák, T. Duchoň, M. Vorokhta, M. Aulická, J. Lachnitt, S. Schernich, I. Matolínová, K. Veltruská, T. Skála, D. Mazur, J. Mysliveček, J. Libuda, V. Matolín, Epitaxial cubic Ce2O3 films via Ce-CeO2 interfacial reaction, J. Phys. Chem. Lett. (2013). https://doi.org/10.1021/jz400187j.

[66] A. Dey, S. Krishnamurthy, J. Bowen, D. Nordlund, M. Meyyappan, R.P. Gandhiraman, Plasma Jet Printing and in Situ Reduction of Highly Acidic Graphene Oxide, ACS Nano

(2018). https://doi.org/10.1021/acsnano.8b00903.

[67] G. SURESH, P.N. NIRMALA, Synthesis of barium oxide nanorod by chemical bath deposition, Turkish J. Phys. 36 (2012) 392–397. https://doi.org/10.3906/fiz-1012-59.

[68] G. Jayakumar, A.A. Irudayaraj, A.D. Raj, Particle size effect on the properties of cerium oxide (CeO2) manoparticles synthesized by hydrothermal method, Mech. Mater. Sci. Eng. J. 9 (2017) 2–7. https://doi.org/10.2412/mmse.3.4.481.

[69] M. Zhang, A. Sun, S. Ma, H. Zhang, Y. Dong, B. Xu, The Influence of BaCeO3 Doping on the Oxygen Distribution, Inhomogeneity and Superconducting Properties of YBa2Cu3O7−δ +0.1mol Y2O3 Superconductors, J. Supercond. Nov. Magn. 29 (2016) 107–113. https://doi.org/10.1007/s10948-015-3253-9.

[70] B. Pandit, E.S. Goda, S.F. Shaikh, Electrochemical Deposition Toward Thin Films, in: Simple Chem. Methods Thin Film Depos., 2023. https://doi.org/10.1007/978-981-99-0961-2_6.

[71] B. Pandit, E.S. Goda, M.H. Abu Elella, A. ur Rehman, S. Eun Hong, S.R. Rondiya, P. Barkataki, S.F. Shaikh, A.M. Al-Enizi, S.M. El-Bahy, K. Ro Yoon, One-pot hydrothermal preparation of hierarchical manganese oxide nanorods for high-performance symmetric supercapacitors, J. Energy Chem. 65 (2022) 116–126. https://doi.org/10.1016/j.jechem.2021.05.028.

[72] B. Pandit, S.A. Pande, B.R. Sankapal, Facile SILAR Processed Bi 2 S 3 :PbS Solid Solution on MWCNTs for High-performance Electrochemical Supercapacitor, Chinese J. Chem. 37 (2019) 1279–1286. https://doi.org/10.1002/cjoc.201900222.

[73] Y. Luo, T. Yang, Q. Zhao, M. Zhang, CeO2/CNTs hybrid with high performance as electrode materials for supercapacitor, J. Alloys Compd. (2017). https://doi.org/10.1016/j.jallcom.2017.09.165.

[74] S. Asaithambi, P. Sakthivel, M. Karuppaiah, R. Yuvakkumar, K. Balamurugan, T. Ahamad, M.A.M. Khan, G. Ramalingam, M.K.A. Mohammed, G. Ravi, Preparation of Fe-SnO2@CeO2 nanocomposite electrode for asymmetric supercapacitor device performance analysis, J. Energy Storage 36 (2021) 102402. https://doi.org/10.1016/j.est.2021.102402.

[75] S. Arunpandiyan, S. Bharathi, A. Pandikumar, S. Ezhil Arasi, A. Arivarasan, Structural analysis and redox additive electrolyte based supercapacitor performance of ZnO/CeO2 nanocomposite, Mater. Sci. Semicond. Process. 106 (2020) 104765.

https://doi.org/10.1016/j.mssp.2019.104765.

[76] N. Ahmad, A.A. Alghamdi, H.A. Al-Abdulkarim, G.M. Mustafa, N. Baghdadi, F.A. Alharthi, Structural, morphological, and electrochemical performance of CeO2/NiO nanocomposite for supercapacitor applications, Appl. Sci. (2021). https://doi.org/10.3390/app11010411.

[77] N. Bibi, Y. Xia, S. Ahmed, Y. Zhu, S. Zhang, A. Iqbal, Highly stable mesoporous CeO2/CeS2 nanocomposite as electrode material with improved supercapacitor electrochemical performance, Ceram. Int. 44 (2018) 22262–22270. https://doi.org/10.1016/j.ceramint.2018.08.348.

[78] B. Pandit, C.D. Jadhav, P.G. Chavan, H.S. Tarkas, J. V. Sali, R.B. Gupta, B.R. Sankapal, Two-Dimensional Hexagonal SnSe Nanosheets as Binder-Free Electrode Material for High-Performance Supercapacitors, IEEE Trans. Power Electron. 35 (2020) 11344–11351. https://doi.org/10.1109/TPEL.2020.2989097.

[79] Y. Li, L. Cao, L. Qiao, M. Zhou, Y. Yang, P. Xiao, Y. Zhang, Ni–Co sulfide nanowires on nickel foam with ultrahigh capacitance for asymmetric supercapacitors, J. Mater. Chem. A 2 (2014) 6540–6548. https://doi.org/10.1039/C3TA15373H.

[80] W. Lei, V.N. Mochalin, D. Liu, S. Qin, Y. Gogotsi, Y. Chen, Boron nitride colloidal solutions, ultralight aerogels and freestanding membranes through one-step exfoliation and functionalization, Nat. Commun. (2015). https://doi.org/10.1038/ncomms9849.

[81] H. Chen, J. Jiang, L. Zhang, D. Xia, Y. Zhao, D. Guo, T. Qi, H. Wan, In situ growth of NiCo2S4 nanotube arrays on Ni foam for supercapacitors: Maximizing utilization efficiency at high mass loading to achieve ultrahigh areal pseudocapacitance, J. Power Sources 254 (2014) 249–257. https://doi.org/10.1016/j.jpowsour.2013.12.092.

[82] W. Du, Z. Zhu, Y. Xu, Z. Zhang, X. Xiong, P. Geng, H. Pang, High-performance asymmetric full-cell supercapacitors based on CoNi2S4 nanoparticles and activated carbon, J. Solid State Electrochem. 19 (2015) 2177–2188. https://doi.org/10.1007/s10008-015-2858-z.

[83] Y. Zhu, Z. Wu, M. Jing, X. Yang, W. Song, X. Ji, Mesoporous NiCo2S4 nanoparticles as high-performance electrode materials for supercapacitors, J. Power Sources (2015). https://doi.org/10.1016/j.jpowsour.2014.09.144.

[84] T.M. Masikhwa, F. Barzegar, J.K. Dangbegnon, A. Bello, M.J. Madito, D. Momodu, N.

Manyala, Asymmetric supercapacitor based on VS2 nanosheets and activated carbon materials, RSC Adv. (2016). https://doi.org/10.1039/c5ra27155j.

[85] Z. Fan, J. Yan, T. Wei, L. Zhi, G. Ning, T. Li, F. Wei, Asymmetric supercapacitors based on graphene/MnO2 and activated carbon nanofiber electrodes with high power and energy density, Adv. Funct. Mater. (2011). https://doi.org/10.1002/adfm.201100058.

[86] T. Brousse, P.-L. Taberna, O. Crosnier, R. Dugas, P. Guillemet, Y. Scudeller, Y. Zhou, F. Favier, D. Bélanger, P. Simon, Long-term cycling behavior of asymmetric activated carbon/MnO2 aqueous electrochemical supercapacitor, J. Power Sources 173 (2007) 633–641. https://doi.org/10.1016/j.jpowsour.2007.04.074.

Table 1: Comparison of electrochemical characteristics of BaO-CeO_2 with other reported composite of cerium oxide and barium oxide-based nanocomposites in aqueous electrolyte.

Sr. No.	Electrode	Method	Morphology	SC [a] (F/g)	Stability		Ref.
					R [b] (%)	Cycles	
1.	PANI/PBF-NPs	Hydrothermal	Three-dimensional network	310	–	–	[11]
2.	MnO_2-CuO-BaO	Hydrothermal	Spherical shaped	198	–	–	[12]
3.	$BaMnO_3$	Solution combusted	spherical grained particles	173.1	93.9	500	[13]
4.	CeO_2	Combustion synthesis	Soapsuds	134.6	92.5	1000	[16]
5.	CeO_2-MnO_2/RGO	Hydrothermal	Nanorod	315.13	90.4	1000	[17]
6.	α-Fe_2O_3@CeO_2	Simple centrifuged	Nano-spear	168	50	2000	[18]
7.	CeO_2/Ce_2O_3	Hydrothermal	–	1027	85	3000	[19]
8.	Ag/CeO_3/rGO	Hydrothermal	Rippled silk veil waves	710.4	73	3000	[21]

9.	PANI/rGO/CeO_2	High yield synthesis	Nano-spear like morphology	684	92	6000	[22]
10.	CeO_2/CNTs	Hydrothermal	Nano-spear clustered	818	95.3	2000	[73]
11.	Fe-SnO_2@CeO_2	Co-precipitation	Nano-spear	348	50	2000	[74]
12.	ZnO/CeO_2	Simple precipitation	Sphere	495.4	95.6	2000	[75]
13	CeO_2/NiO	Hydrothermal	Cauliflower	8.42	−		[76]
14.	CeO_2/CeS_2	Hydrothermal	Cubical and spherical	420	87	1000	[77]
15.	**BaO-CeO_2**	**SILAR**	**Crinum Asiaticum Flower**	**880**	**97**	**6500**	**Present work**

[a] SC= Specific capacitance.

[b] R= Retention.

Table 2: Comparison of BaO-CeO_2//AC ASSD device with another activated carbon-based asymmetric supercapacitor device.

Sr. No.	Asymmetric Solid-state Device	SC [a] (F/g)	SE [b] (Wh/kg)	SP [c] (kW/kg)	Stability		Ref.
					R [d] (%)	Cycles	
1.	Bi_2CuO_4//AC	98.7	30.1	2.08	98.15	5,000	[2]
2.	Ni-Co sulfide nanowire arrays//AC	–	25	0.447	82	1,000	[79]
3.	$Ni_{1.5}Co_{1.5}S_4$//reduced graphene oxide	113	37.6	0.775	90.5	5,000	[80]
4.	$NiCo_2S_4$ nanotube arrays//reduced graphene oxide	197	31.5	0.156	52.6	150	[81]
5.	Mesoporous $NiCo_2S_4$ nanoparticles//AC	–	28.3	0.245	91.7	5,000	[82]
6.	$CoNi_2S_4$ nanoparticles//AC	163.9	53.1	0.763	–		[83]
7.	VS_2//AC	42	42	0.7	99	5,000	[84]
8.	Graphene/MnO_2//ACN	51.1	51.1	–	97	1,000	[85]
9.	AC//MnO	10	10	16	27	195,000	[86]
10.	**BaO-CeO_2//AC**	**213**	**17.8**	**6.8**	**98**	**5,500**	**Present work**

[a] SC= Specific capacitance.

[b] SE= Energy density.

[c] SP= Power density.

[d] R= Retention.